Available online at www.sciencedirect.com
ScienceDirect
International Journal of Multiphase Flow 34 (2008) 894–903
International Journal of Multiphase Flow
www.elsevier.com/locate/ijmulflow

Study of the rotational diffusivity coefficient of fibres in planar contracting flows with varying turbulence levels

Marko Hyensjö [a,b,*], Anders Dahlkild [b]

[a] Metso Paper Karlstad AB, P.O. Box 1014, SE 651 15 Karlstad, Sweden
[b] Department of Mechanics, Royal Institute of Technology KTH, SE-100 44 Stockholm, Sweden

Received 19 June 2007; received in revised form 16 October 2007
Available online 20 February 2008

Abstract

The Fokker–Planck equation is solved by describing the evolution of a 3D fibre orientation state along a planar contraction. A constant value of the effective rotational diffusion coefficient was determined for four different turbulent flow cases in planar contractions, reported experimentally in the literature. Two hypotheses for the non-dimensional rotational diffusivity are presented, each based on two different turbulent time scales, i.e. the Kolmogorov time scales and the time scale associated with large energy bearing eddies. These hypotheses are dependent on either the Reynolds number, based on the Taylor micro-scale, and/or a non-dimensional fibre length. The hypothesis, based on the assumption of long fibres, $L_f/\eta \gtrsim 25$, compared to the Kolmogorov scale and in the limit of large Re_λ seems to capture the basic trends presented in the literature. This hypothesis has also the feature of predicting effects of varying fibre length within certain limits. Accordingly, by modeling the variation of turbulent quantities along the contraction in a CFD analysis, local values of rotational diffusivity can be evaluated with the mentioned hypothesis, based on either Kolmogorov time scale or Eulerian integral time scale.

Keywords: Fokker–Planck equation; Fibre; Orientation; Anisotropy; Turbulence; Dispersion; Modelling

1. Introduction

Many industrial processes and applications utilize the benefits of turbulence and an accelerating flow for certain quality achievements. In, for example, the paper manufacturing process, the introduction of turbulence is proven to break agglomerates of cellulose fibres, producing a paper sheet determined by the local basis weight variation, or fibre/agglomerates distribution, up to a wavelength of 40 mm. This in turn ensures good mechanical properties of the paper sheet, e.g. Andersson and Steen (1962) and Norman and Söderberg (2001). A typical length of cellulose fibre is between 1 and 3 mm, depending on the origin of and the type of tree. In the so-called forming section of a paper machine, the dilute fibre suspension is accelerated by passing through a contracting planar channel, i.e. the headbox, and evenly spreads out as a jet, at speeds up to 35 m/s, onto a moving fabric or into a gap between two moving fabrics. Many of the final paper properties are based upon the state of the fibre suspension in the early stage of the process, e.g. Norman and Söderberg (2001). As the jet hits the moving fabric, the state, or the history, of this jet is essential. The jet is formed in the contraction called a headbox. The headbox ensures that the jet exits the headbox within a specific state, depending on the type of paper being produced. The interaction between this jet and the moving fabric(s) is a main feature for achieving good formation and fibre orientation. For example, in high speed printing it is desirable to have high tensile strength in the direction of the paper feed. For other applications, such as sack paper, a uniform distribution and orientation distribution

* Corresponding author. Address: Metso Paper Karlstad AB, P.O. Box 1014, SE 651 15 Karlstad, Sweden. Tel.: +46 54171214; fax: +46 54177880.
E-mail address: marko.hyensjo@metso.com (M. Hyensjö).

0301-9322/$ - see front matter © 2008 Elsevier Ltd. All rights reserved.
doi:10.1016/j.ijmultiphaseflow.2008.02.005

of the fibres is required. The state of the jet can be modified in various ways. One way is to vary the contraction ratio, i.e. the ratio between the inlet height and the outlet height of the contracting channel. Increasing the contraction ratio is known to significantly increase the fibre alignment, e.g. Ullmar (1997, 1998) and Zhang (2001). This can essentially change the final paper properties, e.g. Nordström and Norman (1994) and Söderberg and Kiviranta (2003). A study made by Olson and Kerekes (1998) and Olson (2001) imposed fibre motion, both translational and rotational, in fluid flow. The flow is described by a stochastic series of independent Fourier modes, reproduced by the Kraichnan energy spectrum, which represents low Reynolds number turbulence. Fibres are furthermore described as rigid, thin and inertialess. Olson and Kerekes (1998) and Olson (2001) concluded that the dispersion coefficients decrease as the ratio of fibre length to Lagrangian integral length scale of the turbulence decrease. The work by Shin and Koch (2005), hereafter referred to as S&K, uses DNS simulation of fully developed isotropic turbulence for studying the translational and rotational motions of fibre with the slender-body theory, e.g. Batchelor, 1970 and Cox (1970). In the study by S&K, the measure of rotational motion is described by the variance of the fibre rotation rate. In the range of Reynolds number considered by S&K, the rotary dispersion coefficient is influenced by the scales of turbulence, i.e. between the Kolmogorov and the Integral time scales. Earlier modelling studies have neglected the influence of turbulence in an accelerated fluid flow, e.g. Akbar and Altan (1992), Olson (2002) and Zhang (2001). Later, the rotational dispersion coefficient has been related to turbulence quantities, cf. Krushkal and Gallily (1988), Olson and Kerekes (1998) and Olson (2001). Recent experimental and computational work by Parsheh et al. (2005, 2006), correlated the rotational dispersion coefficient with turbulent properties on the centreline of a plane contraction. The rotational dispersion coefficient, principally based on the turbulence intensity, is model fitted to the evolution of the fourth moment of the fibre orientation in the contraction.

In this study, assuming an inertialess particle following a central streamline, only the rotational dispersion is taken into consideration. The steady-state Fokker–Planck equation is solved by describing the evolution of a 3D fibre orientation state along a planar contraction, e.g. Advani and Tucker (1987). This has earlier been assumed as planar problems in the studies by, e.g. Hyensjö et al. (2007), Olson et al. (2004) and Parsheh et al. (2005). The four experimental flow cases compared in this paper, differentiated by the level of turbulent energy entering a planar contraction, are described in Parsheh et al. (2005) and Ullmar (1997). A constant value of rotational diffusivity coefficient will be fitted to the respective flow cases, and a scaling evaluation of two different hypotheses, expressed in different time scales, associated with turbulence, is carried out. The time scales considered here are the Kolmogorov and the Eulerian integral time scales.

2. Formulation

For a general description of the fibre orientation state, we used the probability density distribution function for fibre orientation, i.e. $\Psi(x_1, x_2, \phi_1, \theta_1)$. The evolution of Ψ along the planar contraction is described by the steady-state Fokker–Planck equation, e.g. Advani and Tucker (1987) and Eq. (1):

$$U_1\frac{\partial \Psi}{\partial x_1}+U_2\frac{\partial \Psi}{\partial x_2}=\frac{1}{\sin\theta_1}\frac{\partial}{\partial \phi_1}\left(D_r\frac{1}{\sin\theta_1}\frac{\partial \Psi}{\partial \phi_1}-\sin\theta_1\dot{\phi}_1\Psi\right)+\frac{1}{\sin\theta_1}\frac{\partial}{\partial \theta_1}\left(D_r\sin\theta_1\frac{\partial \Psi}{\partial \theta_1}-\sin\theta_1\dot{\theta}_1\Psi\right). \tag{1}$$

This requires the simultaneous consideration of the azimuthal angle, ϕ_1, and the polar orientation angle, θ_1, cf. Fig. 1. The cartesian velocity components of the average flow field are U_1 and U_2. Rotational velocities due to the mean velocity gradients of the fibre orientational angles, ϕ_1 and θ_1, in (1) are denoted $\dot{\phi}_1$ and $\dot{\theta}_1$, respectively. An example of a model for the rotational diffusivity, D_r, for laminar flow due to hydrodynamic interactions between fibres can be found in the work by Folgar and Tucker (1984) and Koch (1995). The rotational diffusivity, D_r, in (1) of the present work is rather due to the turbulent fluctuations of the flow field. However, in our simulation we considered a dilute fibre suspension which excludes any fibre–fibre hydrodynamic interaction. This is also the flow and concentration regime considered in the experimental works by Parsheh et al. (2005, 2006) and Ullmar (1997, 1998), to which our simulations are compared. The rotational diffusivity, D_r, is kept constant throughout the flow field at a value related to the fibre length and the overall turbulent properties of the flow, as will be described later in detail.

For the rotational velocities induced by the average flow field, we use the fundamental study of a single undisturbed fibre by Jeffery (1922) which is here applied in the limit of an infinitely thin fibre, i.e. large aspect ratio. Equations for the rotational velocities for the 3D orientation vector can also be found in Goldsmith and Mason (1967), and for a large aspect ratio of the fibre these can be reduced to

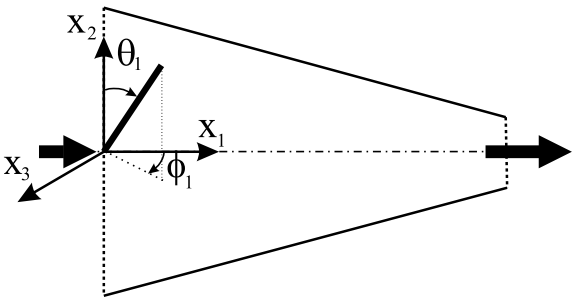

Fig. 1. Schematic view of the planar contraction with the definition of coordinate system and fibre orientation angles.

$$\dot{\phi}_1 = -\sin 2\phi_1 \frac{1}{2}\frac{\partial U_1}{\partial x_1} - \sin\phi_1 \frac{\cos\theta_1}{\sin\theta_1}\frac{\partial U_1}{\partial x_2}, \tag{2}$$

$$\begin{aligned}\dot{\theta}_1 = {} & \cos\phi_1 \frac{1}{2}\left(\frac{\partial U_1}{\partial x_2} - \frac{\partial U_2}{\partial x_1}\right) + \cos\phi_1 \cos 2\theta_1 \\ & \times \frac{1}{2}\left(\frac{\partial U_1}{\partial x_2} + \frac{\partial U_2}{\partial x_1}\right) + \sin 2\theta_1 \frac{1}{2}\left(\frac{\partial U_1}{\partial x_1} - \frac{\partial U_2}{\partial x_2}\right) \\ & + (\cos 2\phi_1 - 1)\sin 2\theta_1 \frac{1}{4}\frac{\partial U_1}{\partial x_1}.\end{aligned} \tag{3}$$

Eqs. (2) and (3) are expressed in mean velocity gradients applied on the center of the fibre. We consider the evolution of Ψ along the centreline of the contraction, i.e. $x_2 = 0$, where the mean velocity field is taken from inviscid theory and is given by $U_1 = U_{1,0}/(1 - x_1/r_0)$, $U_2 = 0$, where r_0 is the distance from the inlet to the apex of the contraction. Eq. (1) with (2) and (3), using incompressibility and symmetry conditions for the velocity gradients at the centreline, then gives

$$\begin{aligned}U\frac{\partial \Psi}{\partial x} = {} & \frac{1}{\sin\theta_1}\frac{\partial}{\partial\phi_1}\left(\frac{1}{Pe_{r,0}}\frac{1}{\sin\theta_1}\frac{\partial\Psi}{\partial\phi_1} + \sin\theta_1 \sin 2\phi_1 \frac{1}{2}\frac{\partial U}{\partial x}\Psi\right) \\ & + \frac{1}{\sin\theta_1}\frac{\partial}{\partial\theta_1}\left(\frac{1}{Pe_{r,0}}\sin\theta_1\frac{\partial\Psi}{\partial\theta_1} - \sin\theta_1\sin 2\theta_1 \right. \\ & \left. \times \left(\frac{3}{4} + \frac{1}{4}\cos 2\phi_1\right)\frac{\partial U}{\partial x}\Psi\right),\end{aligned} \tag{4}$$

where non-dimensional parameters $U = U_1/U_0$, $x = x_1/r_0$ and $Pe_{r,0} = U_0/(r_0 D_r)$ are used. Due to the symmetry of Ψ with respect to $\phi_1 = 0$ (and $\phi_1 = \pi$), we consider only the interval $\phi_1 \in [0, \pi]$. The boundary conditions at $\phi_1 = 0, \pi$ are then $\frac{\partial\Psi}{\partial\phi_1} = 0$. For numerical implementation, we also note that this implies zero flux conditions in the ϕ_1-direction:

$$\left[D_r \frac{1}{\sin\theta_1}\frac{\partial\Psi}{\partial\phi_1} - \sin\theta_1\dot{\phi}_1\Psi\right]_{\phi_1=0,\pi} = 0 \tag{5}$$

since $\dot{\phi} = 0$ at $\phi_1 = 0, \pi$. For numerical implementation of the flux in the θ_1-direction at $\theta_1 = 0, \pi$ we note that from the definition

$$\left[D_r \sin\theta_1 \frac{\partial\Psi}{\partial\theta_1} - \sin\theta_1\dot{\theta}_1\Psi\right]_{\theta_1=0,\pi} = 0 \tag{6}$$

i.e. the flux is zero as long as $\frac{\partial\Psi}{\partial\theta_1}$ is finite. In the present formulation, the solution yields the result $\frac{\partial\Psi}{\partial\theta_1} = 0$ at $\theta_1 = 0, \pi$.[1]

[1] This can also be derived from the consideration of the symmetry with respect to $\theta_1 = \pi/2$, which was, however, not made use of explicitly in the formulation of the boundary condition. Then for any given orientation (ϕ_1^*, θ_1^*) we have $\Psi_{\theta_1}(\phi_1^*, \theta_1^*) = -\Psi_{\theta_1}(\phi_1^*, \pi - \theta_1^*)$, where Ψ_{θ_1} denotes the partial derivative of Ψ with respect to θ_1. Also, since the fibre is assumed symmetrical with respect to its centre of mass, we must have $\Psi(\phi_1^*, \pi - \theta_1^*) = \Psi(\phi_1^* + \pi, \theta_1^*)$. Thus, $-\Psi_{\theta_1}(\phi_1^*, \pi - \theta_1^*) = \Psi_{\theta_1}(\phi_1^* + \pi, \theta_1^*)$. The symmetry condition then yields $\Psi_{\theta_1}(\phi_1^*, \theta_1^*) = \Psi_{\theta_1}(\phi_1^* + \pi, \theta_1^*)$. On the other hand, due to continuity of the derivative of Ψ along a meridian across the poles at $\theta_1^* = 0, \pi$ we must have $\Psi_{\theta_1}(\phi_1^*, \theta_1^* = 0, \pi) = -\Psi_{\theta_1}(\phi_1^* + \pi, \theta_1^* = 0, \pi)$, which together with the symmetry condition applied at the poles yield $\Psi_{\theta_1}(\phi_1^*, \theta_1^* = 0, \pi) = 0$.

At the inlet of the contraction, we assume a homogeneous fibre orientation distribution

$$\Psi_{x_1=0} = \frac{1}{2\pi}, \tag{7}$$

where at all positions

$$\int_0^\pi \int_0^\pi \Psi \sin\theta_1 \, d\theta_1 \, d\phi_1 = 1. \tag{8}$$

The diffusivity coefficient, D_r, is assumed constant throughout the contraction. We show that our simulation of the evolution of the fibre orientation distribution can reproduce an anisotropy in fair agreement with the chosen experiments from the literature by adjusting the value of D_r. The measure of anisotropy used is the first component of the fourth-order planar orientation tensor, cf. Parsheh et al. (2005), in the (x_1, x_3)-plane

$$a_{1111} = \int_0^\pi p_1^4 \Psi^p \, d\phi_1 = \int_0^\pi \cos^4\phi_1 \Psi^p \, d\phi_1, \tag{9}$$

where $\bar{p} = (\cos\phi_1, \sin\phi_1)$, and Ψ^p is the planar orientation distribution

$$\Psi^p = \int_0^\pi \Psi \sin\theta_1 \, d\theta_1 \tag{10}$$

which according to (8) satisfies $\int_0^\pi \Psi^p \, d\phi_1 = 1$. One may note here that our formulation is more general than that considered by Parsheh et al. (2005) since we do not assume the distribution function to be planar but use the full 3D distribution function Ψ. The planar distribution Ψ^p is obtained from the projection of the fibres in the (x_1, x_3)-plane. The values of D_r used in the simulation that give the best fit of a_{1111} for each experiment chosen for comparison are determined. We then seek a relation between the overall turbulent level of each experiment and D_r. We have chosen the state at the inlet of the contraction to characterize the overall turbulent levels. The motivation for this, and the choice of a constant diffusivity, D_r, is twofolded. First, differences in turbulence levels between the individual cases are generally higher than the differences in turbulence level between the inlet and the outlet for each case. Secondly, the rotational Peclet-number, $Pe_r = \frac{\partial U_1}{\partial x_1}/D_r$, increases rapidly along the contraction, see Fig. 2, whereby the diffusivity has its major role at the beginning of the contraction. The properties that we need to identify at the inlet for each case are streamwise mean velocity, $U_{1,0}$, turbulent kinetic energy, k_0, and turbulent dissipation rate, ϵ_0. The experiments considered are two cases from Parsheh et al. (2005), i.e. Cases 1 and 2, and two cases described in a study by Ullmar (1997), i.e. Cases 3 and 4. The first study, Cases 1 and 2, describes a mesh-generated turbulence that changes by means of increasing the flow rate. In Cases 3 and 4, the turbulence is generated by a bundle of pipes, i.e. 3×7 pipes, with a round-to-round sudden pipe expansion followed by a round-to-square step, leading to a square shaped outlet, entering a short straight channel before the contraction. This will generate much higher levels

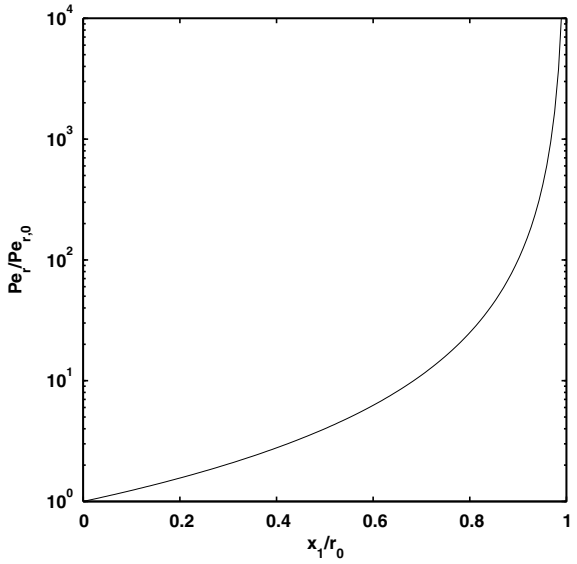

Fig. 2. The rotational Peclet-number evaluation normalized with the inlet value as a function of the normalized x_1 coordinate with r_0.

of turbulence than that in Cases 1 and 2. For Case 1, the level of kinetic energy of turbulence, k_0, is estimated with an approximation of decaying isotropic turbulence, from a uniform grid in a straight channel, given by Roach (1987) together with the experimental data provided by Parsheh et al. (2005) to be

$$k_0 = \frac{3}{2}U_0^2\left(1.2\left(\frac{l}{d}\right)^{-\frac{5}{7}}\right)^2, \tag{11}$$

where 1.2 is a constant based on the grid geometry and has been fitted to the experimental result for Case 1, l is the downstream position from the grid, d is the grid bar width of the mesh, and U_0 is the streamwise velocity upstream of the contraction. Turbulence entering into a planar contraction will continue to decay as isotropic turbulence, according to the decaying law, for some distance, before any anisotropic effects become significant, e.g. Brown et al. (2006), Parsheh et al. (2005, 2006) and Roach (1987). Additionally, the results by Brown et al. (2006) showed that the anisotropy of the flow reaches a peak value at $2.5 < C < 3.5$, whereafter it returns almost completely to an isotropic state inside the latter part of the contraction. For Case 2, it was assumed that the same decaying law specified in (11) was valid. Based on the equation for the mean kinetic energy of turbulence, and the assumption of decaying isotropic turbulence, i.e. there is no production of turbulence and the mean flow is constant, the dissipation rate of turbulent energy at the inlet of the contraction, ϵ_0, can be estimated, for Case 1 and Case 2, together with (11) from

$$U\frac{\partial k_0}{\partial x_1} = -\epsilon_0. \tag{12}$$

The estimation of turbulence levels for Cases 3 and 4, i.e. Ullmar (1997, 1998), has been made with CFD modelling. Mean quantities of k and ϵ from simulations just before the contraction were used for the evaluation of the inlet value. The Reynolds number based on the mean flow is defined as $Re = U_0 h_0/\nu$.

To describe the relations between D_r and k and ϵ, we follow the notation by S&K who express D_r in terms of the fibre orientation auto-correlation integral time, T_p as

$$D_r = \frac{1}{2T_p}, \tag{13}$$

where T_p is expressed in terms of two different scalings

$$T_p = \tau_\eta f_\eta(Re_\lambda, L_f/\eta) = \tau_\Lambda f_\Lambda(Re_\lambda, L_f/\Lambda). \tag{14}$$

The first one is associated with the Kolmogorov time scale

$$\tau_\eta = \left(\frac{\nu}{\epsilon}\right)^{\frac{1}{2}} \tag{15}$$

and the second one with the Eulerian integral time scale

$$\tau_\Lambda = \frac{\Lambda}{u_{\rm rms}}, \tag{16}$$

where $u_{\rm rms} = \sqrt{\frac{2k_0}{3}}$. The non-dimensional functions f_η and f_Λ are generally dependent on the Reynolds number based on the Taylor micro-scale, $\lambda = \sqrt{15}u_{\rm rms}\sqrt{\nu/\epsilon_0}$

$$Re_\lambda = \frac{u_{\rm rms}\lambda}{\nu} \tag{17}$$

and the non-dimensional fibre lengths L_f/η, L_f/Λ scaled with the Kolmogorov length scale

$$\eta = (\nu^3/\epsilon)^{1/4} \tag{18}$$

and the turbulent Eulerian integral length scale, Λ, respectively. We will assume here that Λ is of the same order of magnitude as the large energy bearing eddies in turbulence, given by

$$\Lambda \approx L \equiv \frac{k_0^{\frac{3}{2}}}{\epsilon_0}. \tag{19}$$

3. Analysis

The Fokker–Planck equation, (4), is solved by the multiphysics program COMSOL Multiphysics ver.3.3, which is a FEM-based solver. Mesh independent solutions are achieved for all the cases solved in this study. Since there is a lack of measured turbulent quantities for Cases 3 and 4, i.e. Ullmar (1997, 1998), the levels of turbulence kinetic energy, k_0, and dissipation rate of kinetic energy, ϵ_0, are estimated by CFD modelling. The axisymmetric sudden pipe expansion, called the turbulence generator, and a short straight channel section, just before the contraction, were modeled with the omega–Reynolds Stress Turbulence Model, provided by the ANSYS CFX v11 code. Due to symmetrical reasons, a quarter of each of four the neighboring pipes, i.e. 2×2 pipes, were considered in the CFD-model.

Based on the values of D_r determined for the different flow cases and the specific sets of the overall turbulent

properties of these flow cases, we seek approximations to the functions, f_η and f_Λ, in certain limits of the parameters. To do this, we let ourselves be guided by the DNS results from S&K describing the fibre orientation auto-correlation time, T_p, as a function of fibre length, shown in Fig. 3 in two different non-dimensional units. In Fig. 3a the Kolmogorov time and length scales are used for non-dimensionalization, whereas in Fig. 3b Eulerian integral time and length scales are used. S&K draw the conclusion that neither Kolmogorov scales or Eulerian integral scales collapse the data independently of Reynolds number, Re_λ. They specifically note that whereas the Eulerian integral time, τ_{Λ_1}, actually is similar in magnitude to T_p, the Kolmogorov time scale, τ_η, is substantially smaller. Fig. 3b also shows the quadratic asymptotes for short fibres fitted by S&K according to

$$\frac{T_p}{\tau_{\Lambda_1}} = b_{p,0} + b_{p,2}\left(\frac{L_f}{\Lambda_1}\right)^2. \tag{20}$$

The coefficients $b_{p,0}$ and $b_{p,2}$ are indeed dependent on Re_λ, where the trend is that $b_{p,0}$ decreases and $b_{p,2}$ increases with Re_λ. Based on the 3D energy spectrum of the DNS generated homogeneous isotropic turbulent flow by S&K, the Eulerian integral length scale, Λ_1, in (20) and Fig. 3b, is defined as the two-point velocity correlation in the longitudinal direction, i.e. x_1-direction (note that in the present work, the Eulerian integral length scale is defined by (19)). S&K also give the Re_λ-dependent quadratic asymptotes for short fibres in the Kolmogorov scaling, but these will not be relevant to our parameter regime. In all, S&K conclude that their expectation, that T_p/τ_η is a function, f_η, only of L_f/η, would be possible only at very high Re_λ and with large values of f_η. Guided by the data shown in Fig. 3a and b, we present two hypotheses for T_p. The first hypothesis is based on the quadratic asymptotes for short fibres using the Eulerian integral scaling. In a first approximation, for very small values of L_f/Λ_1, the second term of (20) can be neglected, which according to Fig. 3b seems reasonable at least for, say, $L_f/\Lambda_1 < 0.3$. The upper limit in L_f/Λ_1 for this approximation is lower for larger Re_λ, but the data of our investigation also follow this trend. The remaining coefficient, $b_{p,0}$, is still dependent of Re_λ and we make the assumption

$$f_\Lambda^{\mathrm{I}} = \frac{1}{(a_1 + b_1 Re_\lambda)}, \tag{21}$$

where a_1 and b_1 are constants independent of L_f/Λ. The second hypothesis for T_p considers long fibres in terms of the Kolmogorov scaling and in the limit of large Re_λ. From Fig. 3a, we observe that for $L_f/\eta > 25$, and data of Reynolds numbers in the interval $30 < Re_\lambda < 50$, the dependence on Re_λ is much weaker and the data collapse approximately on a straight line, as indicated. Our simulations are in the range of $Re_\lambda = 50 - 250$. Thus, we assume

$$f_\eta^{\mathrm{II}} = a_2 + b_2\frac{L_f}{\eta}, \tag{22}$$

where a_2 and b_2 are constants independent of Re_λ. As commented by S&K, f_η may be expected to be independent of $Re_\lambda \gg 1$ as the largest velocity gradients occur in Kolmogorov eddies, although their DNS results do indicate an overall Re_λ-dependence. (One may note that such linear dependence on fibre length, $L_f/\eta > 20$, was obtained by S&K for the zero-crossing time of the fibre rotation-rate auto-correlation function normalised with the Kolmogorov time scale, a correlation function that was also found overall independent of Re_λ.) As a complementary part of the

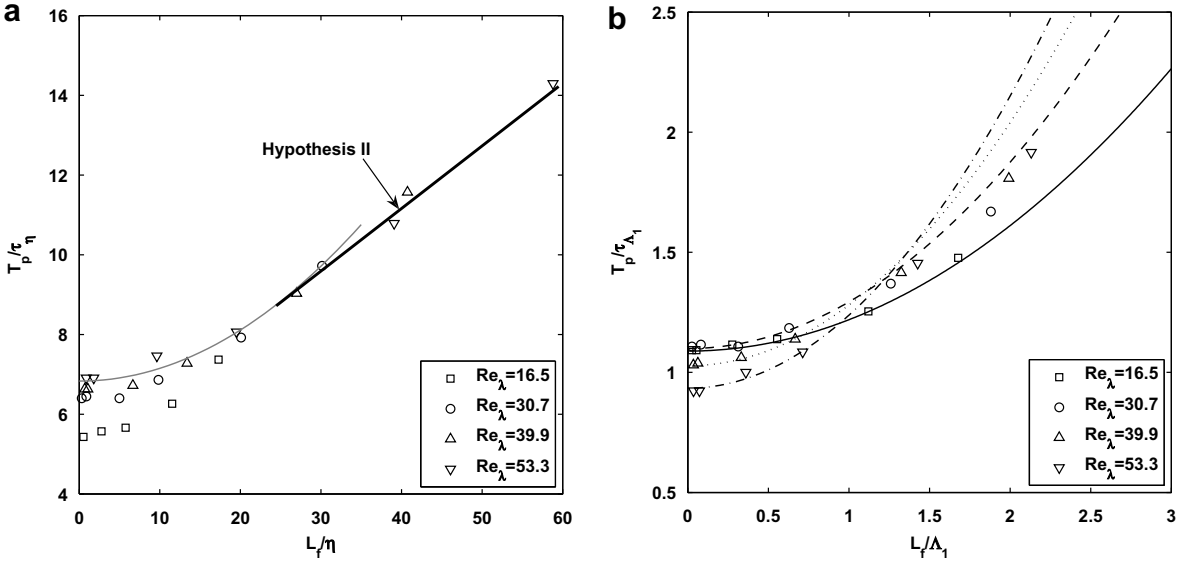

Fig. 3. DNS data for various Re_λ by Shin and Koch (2005) of the integral time for fibre orientation as a function of fibre length with respect to Kolmogorov time and length scales in (a), and Eulerian integral time and length scales in (b). Quadratic asymptotes in (b) of the DNS data according to (20).

Table 1
Summary of the hypotheses

	T_p/τ_η	T_p/τ_Λ	
Hypothesis I	$\frac{3}{2\sqrt{10}}\frac{Re_\lambda}{(a_1+b_1Re_\lambda)}$	$\frac{1}{(a_1+b_1Re_\lambda)}$	a_1 =0.0473 b_1 =0.0052
Hypothesis II	$a_2+b_2\frac{L_f}{\eta}$	$\frac{2\sqrt{10}}{3}\frac{1}{Re_\lambda}\left(a_2+b_2\left(\left(\sqrt{\frac{3}{20}}Re_\lambda\right)^{3/2}\frac{L_f}{\Lambda}\right)\right)$	a_2 =68.23 b_2 =0.3525

second hypothesis for smaller values of L_f/η, one may consider a quadratic asymptote that joins smoothly with (22) at $L_f/\eta = 25$. This is also indicated in Fig. 3a, and would represent the limit for large Re_λ. However, the data we use here do not cover the region $L_f/\eta < 25$. In the following, we also express the first hypothesis in terms of Kolmogorov scaling and the second hypothesis in terms of Eulerian integral scaling. Thus from the first hypothesis we have

$$\frac{T_p}{\tau_\eta}^{\mathrm{I}} = \frac{\tau_\Lambda}{\tau_\eta} f_{\Lambda_1}(Re_\Lambda) = \frac{\tau_\Lambda}{\tau_\eta}\frac{1}{(a_1+b_1Re_\lambda)}. \tag{23}$$

The first factor on the R.H.S. can be expressed as

$$\frac{\tau_\Lambda}{\tau_\eta} = \frac{\Lambda}{u_{\mathrm{rms}}}\left(\frac{\epsilon}{\nu}\right)^{1/2} = \frac{k^{3/2}}{\epsilon}\sqrt{\frac{3}{2k}}\left(\frac{\epsilon}{\nu}\right)^{1/2} = \sqrt{\frac{3}{2}}\frac{k}{\sqrt{\epsilon\nu}}. \tag{24}$$

The Taylor micro-scale Reynolds number, Re_λ, can be rewritten as

$$Re_\lambda = \frac{u_{\mathrm{rms}}\lambda}{\nu} = \left(\lambda = \sqrt{15\frac{2}{3}\frac{k\nu}{\epsilon}}\right) = \sqrt{\frac{20}{3}}\frac{k}{\sqrt{\nu\epsilon}}. \tag{25}$$

(24) can then be expressed in Re_λ as

$$\frac{\tau_\Lambda}{\tau_\eta} = \sqrt{\frac{3}{2}\frac{3}{20}}Re_\lambda = \frac{3}{2\sqrt{10}}Re_\lambda \tag{26}$$

and with (26), (23) can be written as

$$\frac{T_p}{\tau_\eta}^{\mathrm{I}} = \frac{3}{2\sqrt{10}}\frac{Re_\lambda}{(a_1+b_1Re_\lambda)}. \tag{27}$$

Note here that as $Re_\lambda \to \infty$ the ratio $T_p^{\mathrm{I}}/\tau_\eta$ is constant, which is in accordance with the original expectation of S&K, although only valid for $L_f/\Lambda \ll 1$. From the second hypothesis, we get

$$\begin{aligned}\frac{T_p}{\tau_\Lambda}^{\mathrm{II}} &= \frac{\tau_\eta}{\tau_\Lambda} f_{\eta_{\mathrm{II}}}(L_f/\eta) = \frac{\tau_\eta}{\tau_\Lambda}\left(a_2+b_2\frac{L_f}{\eta}\right)\\ &= \frac{\tau_\eta}{\tau_\Lambda}\left(a_2+b_2\left(\frac{L_f}{\Lambda}\frac{\Lambda}{\eta}\right)\right).\end{aligned} \tag{28}$$

Furthermore, the scale ratio between the larger energy bearing eddies, $L = \Lambda$, and the Kolmogorov scale, η, in (28), can also be expressed in Re_λ. With (18), (19) and (25), we have

$$\frac{\Lambda}{\eta} = \frac{k^{3/2}}{\epsilon}\left(\frac{\epsilon}{\nu}\right)^{1/4} = \left(\frac{k}{\sqrt{\nu\epsilon}}\right)^{3/2} = \left(\sqrt{\frac{3}{20}}Re_\lambda\right)^{3/2}. \tag{29}$$

Now with the inverse of (26), and (29), inserted in (28) yields

$$\frac{T_p}{\tau_\Lambda}^{\mathrm{II}} = \frac{2\sqrt{10}}{3}\frac{1}{Re_\lambda}\left(a_2+b_2\left(\left(\sqrt{\frac{3}{20}}Re_\lambda\right)^{3/2}\frac{L_f}{\Lambda}\right)\right). \tag{30}$$

Naturally, this function is also linear in the fibre length which is definitely not the trend for smaller values of L_f/Λ according to Fig. 3b. However, it is overall dependent on Re_λ in agreement with the data of the same figure. A summary of the hypotheses is given in Table 1, where the parameters a_1, b_1, a_2 and b_2 are determined by regression analysis of the results for the diffusivity coefficients, $D_{\mathrm{r}} = \frac{1}{2T_p}$.

4. Results

In Table 2, all the flow cases and their turbulence levels and structures, i.e. scales, entering the contraction and some simulation results, are summarized. For Cases 1 and 2, the respective turbulent kinetic energy, k_0, was expressed from the measured quantity, u_{rms}, by assuming isotropic turbulence, i.e. $k = 3/2u_{\mathrm{rms}}^2$. The experimental measurement of the longitudinal integral length scale for Case 1, by Parsheh et al. (2005), is reported to vary between $2L_f$ at the inlet to $10L_f$ at $C = 8$, with L_f as the fibre length. Our estimation, (19), taken from the energy bearing eddies, L, is about $3L_f$–$10L_f$ at the inlet depending on the Reynolds number. Compared with the integral length scale obtained by S&K, we find from (29) that $(\Lambda/\eta)Re_\lambda^{-3/2} = 0.24$, which is a factor of about three times larger than their value for the larger Reynolds numbers. A constant value of D_{r} was determined by optimizing the agreement of the solution of (4) with the experimental data provided by Parsheh et al. (2005), cf. Fig. 4. The orientation state, as shown in Fig. 4, is illustrated by the fourth moment of the streamwise orientation tensor, a_{1111} given in (9), and is plotted against the contraction ratio, C, defined as the ratio of the local streamwise mean velocity to the inlet streamwise mean velocity, $U_1/U_{1,0}$. A least square optimization method was carried out on all the experimental data along the contraction giving the value of the rotational dispersion coefficient, D_{r}. Starting from a homogeneous inlet condition of the fibre orientation distribution, Case 2 will have a larger value of D_{r} than Case 1 which correlates with the higher turbulence level entering the contraction, cf. Table 2 and Parsheh et al. (2005). Higher levels of turbulence will even out the fibre orienta-

Table 2
Summary of the flow properties at the contraction inlet for the different flow cases

	Case 1	Case 2	Case 3	Case 4
$D_r\left[\frac{1}{s}\right]$	0.38	0.99	1.14	1.98
$Pe_{r,0}$ [−]	1.9	1.46	0.58	0.5
$\epsilon_0\left[\frac{m^2}{s^3}\right]$	3.050×10^{-3}	2.440×10^{-2}	3.315×10^{-2}	1.101×10^{-1}
$k_0\left[\frac{m^2}{s^2}\right]$	1.034×10^{-3}	4.138×10^{-3}	1.041×10^{-2}	2.310×10^{-2}
$U_{1,0}\left[\frac{m}{s}\right]$	0.4375	0.875	0.344	0.516
$u_{rms}\left[\frac{m}{s}\right]$	2.626×10^{-2}	5.252×10^{-2}	8.331×10^{-2}	1.241×10^{-1}
T_0 [%]	6.0	6.0	24.2	24.0
L_f [mm]	3.2	3.2	3.0	3.0
L [mm]	1.091×10^{1}	1.091×10^{1}	3.204×10^{1}	3.188×10^{1}
λ_t [mm]	1.741	1.230	1.674	1.368
η [mm]	0.124	0.073	0.068	0.050
Re [−]	85×10^{3}	170×10^{3}	96×10^{3}	144×10^{3}
Re_λ [−]	51.2	72.4	156.3	190.2
L_f/η [−]	25.8	43.8	44.1	59.5
$L_f/(\Lambda = L)$ [−]	0.29	0.29	0.1	0.1

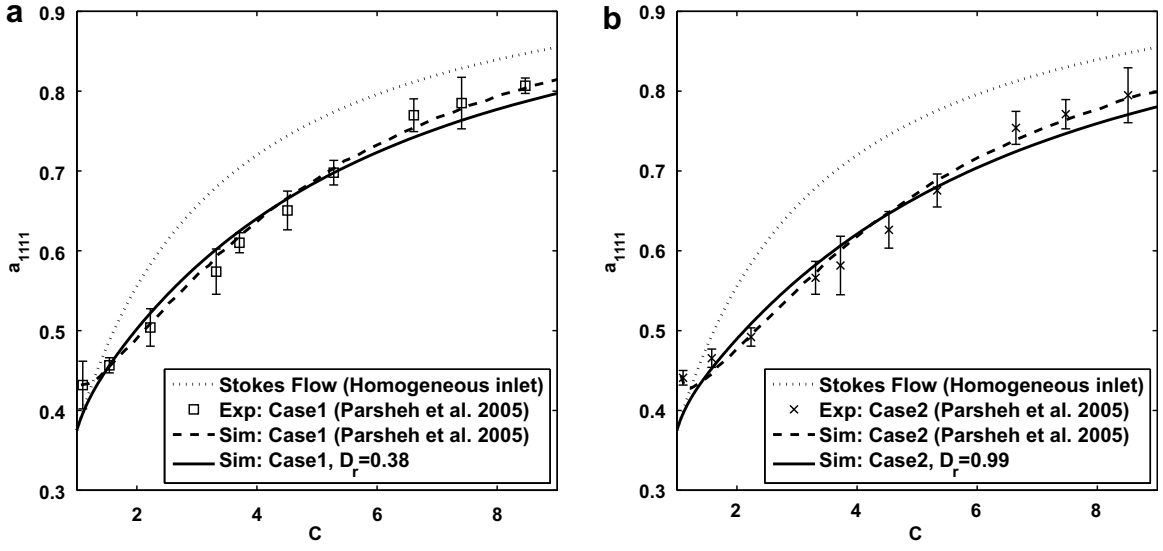

Fig. 4. Development of the fourth moment of the orientation vector along the contraction, experimentally and simulated results by Parsheh et al. (2005), together with results from the present simulation using a fit of a constant value of D_r for the respective flow case.

tion probability function more and decrease the anisotropy, i.e. a_{1111}. Also in Fig. 4, the Stokes flow case is included, i.e. D_r is equal to zero. Fig. 4 also shows the simulated results by Parsheh et al. (2005) for Cases 1 and 2. There are three main differences between our simulation and that of Parsheh et al. (2005). Firstly, the rotational diffusivity in their work is not constant as in ours, but decays exponentially with the contraction ratio at a rate determined by a least-square fit to their experimental data of a_{1111}. Secondly, their initial condition for the probability density distribution function is not a homogeneous one, as here. Instead, the measured planar distribution function at contraction ratio $C = 1.1$ is considered as an initial condition, whereby the simulated value of a_{1111} automatically agrees with the measured one at $C = 1.1$. Finally, their simulations assume a planar distribution, i.e. all fibres are aligned in the azimuthal plane, i.e. $\theta_1 = \pi/2$. In our simulation, we consider the full three dimensional distribution, in which orientations are then consistently projected to get a_{1111}. Overall, our fitted simulations agree reasonably well with the experimental data of Parsheh et al. (2005), despite the simplified initial condition and the use of a constant rotational diffusivity. The experimental results by Ullmar (1997) provided only outlet profiles of the fibre orientation distribution in the contraction. Fig. 5 shows the planar orientation distribution functions of the experimental Cases 3 and 4 as compared to those obtained from the simulation that gives the same value of a_{1111} at the outlet centreline. The specific values of D_r required are summarized in Table 2. Also here the trend is that the higher the turbulence level entering the contraction, the higher the constant value of D_r is required.

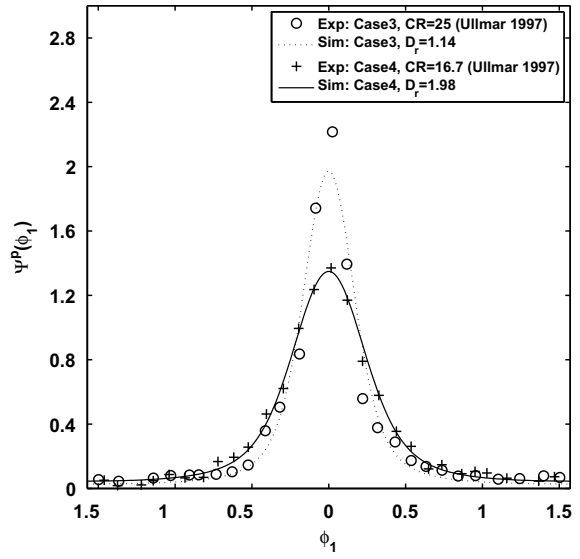

Fig. 5. Constant value approximation of D_r for different contraction ratios, CR, against experimental data provided by Ullmar (1997).

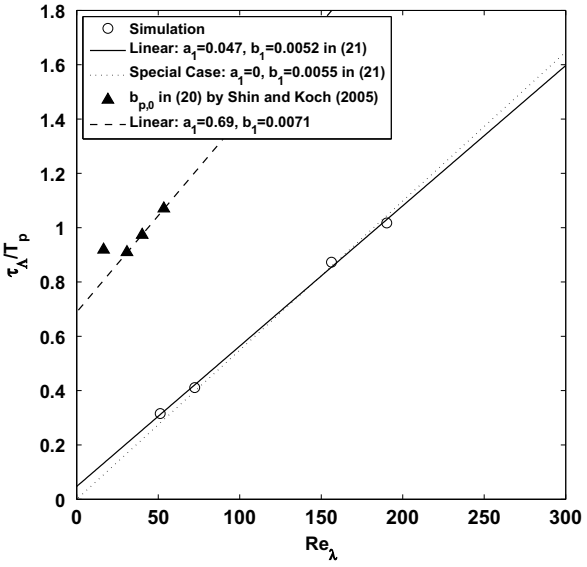

Fig. 6. Determined parameters related with the inverse of (21), showing the Eulerian integral time scale, τ_Λ, related to the fibre orientation integral time scale, T_p, as a function of Re_λ.

To test the first hypothesis, discussed in the previous paragraph, we plot $2D_r\tau_\Lambda = \tau_\Lambda/T_p$ versus Re_λ for the simulation results shown in Fig. 6. The corresponding linear regression line, according to (21), with the parameters, $a_1 = 0.047$ and $b_1 = 0.0052$, is also shown. The good fit illustrates that for the limits of small L_f/Λ, D_r scales in magnitude with the inverse of the Eulerian integral time scale and $D_r\tau_\Lambda$ increases with Re_λ. This trend is also obtained by S&K in their simulations, cf. Fig. 3b. Their values of $1/b_{p,0}$, cf Eq. (20), are also shown in Fig. 6, including a corresponding linear regression line to their data for the larger Reynolds numbers. Also in Fig. 6, a special case of a linear regression line drawn through the origin is shown. This implies a constant value of $T_p^{\mathrm{I}}/\tau_\eta$ independent of Re_λ, cf. (27). Furthermore, as can be seen from (27), $T_p^{\mathrm{I}}/\tau_\eta$ increases with increasing Re_λ and levels out for larger values. In summary, the first hypothesis described, (21), is not able to catch any variations of D_r with different fibre length ratios.

Considering the values of L_f/η in the Cases 1–4 studied, we have $25 \lesssim L_f/\eta \lesssim 60$ and $50 < Re_\lambda < 200$. This is well above the lower limits of L_f/η and Re_λ when T_p/τ_η may be regarded as independent of Re_λ and linear in L_f/η according to the simulations by S&K, cf. Fig. 3a. Considering the second hypothesis in (22), the simulated results with the corresponding linear regression line is illustrated in Fig. 7. The parameters determined are $a_2 = 68.2$ and $b_2 = 0.352$, which gives a good fit. The relative slope, $\frac{1}{f_\eta}\frac{\mathrm{d}}{\mathrm{d}(L_f/\eta)}(f_\eta)$, at $L_f/\eta = 25$ is of the same order of magnitude as that found in the results of S&K, although the values of $T_p^{\mathrm{II}}/\tau_\eta$ are a factor of 10 times larger. The complementary part of the second hypothesis for $L_f/\eta < 25$ and large Re_λ is also given in Fig. 7 as the quadratic asymptote that joins smoothly with (22) at $L_f/\eta = 25$. In Fig. 8, the second hypothesis is shown in terms of the integral scaling, $T_p^{\mathrm{II}}/\tau_\Lambda$, according to Eq. (30). The same qualitative behaviour for curves of different Re_λ as that shown in Fig. 3b is observed. Thus, for the lower values of L_f/Λ, the trend is that higher Re_λ leads to a lower value of f_η, and vice versa for higher values of L_f/Λ. In fact, evaluating the inverse of (30) at $L_f/\Lambda = 0$ gives a linear variation with Re_λ at a slope of 0.007, which is almost identical to that of $b_{p,0}$ as shown in Fig. 6 obtained in S&K. For small values of L_f/Λ the complementary part of the second hypothesis, also indicated in Fig. 8, can be used to get results in a qualitative agreement with the quadratic asymptotic behaviour as shown in Fig. 3b. Note that the difference in the definition

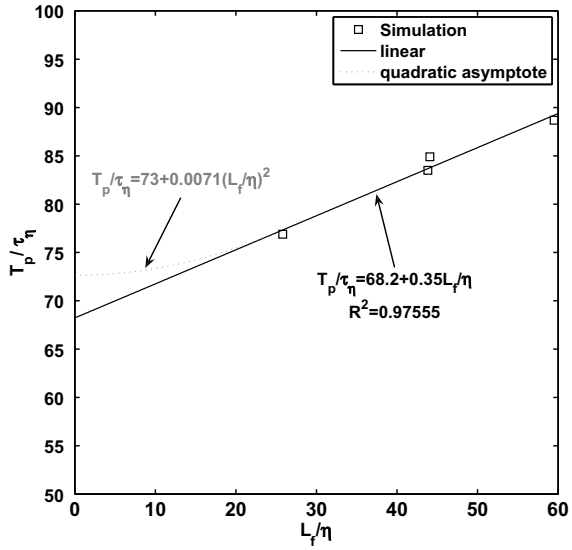

Fig. 7. Optimized parameters, a_2 and b_2, according to (22) showing the fibre orientation integral time scale, T_p, related to the Kolmogorov time scale, τ_η, as a function of L_f/η, and the complementary quadratic asymptote for $L_f/\eta < 25$.

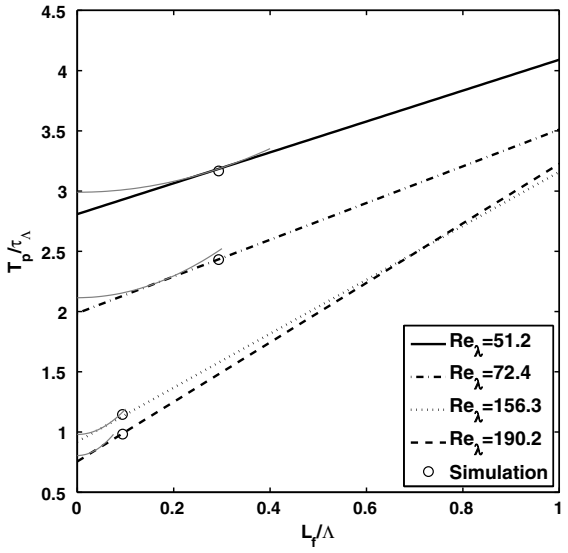

Fig. 8. The fibre orientation integral time scale, T_p, related to the Eulerian integral time scale, τ_Λ, as a function of L_f/Λ with constant values of Re_λ, according to (30), and with the respective complementary quadratic asymptotes.

of the integral length scale compared to that of S&K is compensated for by using an interval of L_f/Λ between 0 and 1 shown in Fig. 8, rather than L_f/Λ_1 from 0 to 3 as shown in Fig. 3b.

5. Conclusions

The Fokker–Plank equation for the orientation distribution function of slender fibres was solved for turbulent flow along the centreline of a planar contraction with mean velocities from inviscid theory, and a constant rotational diffusivity coefficient, D_r. It was demonstrated that the constant value of the rotational diffusivity coefficient could be adjusted to account for the variation of orientation anisotropy at various levels of turbulence entering the contraction in four chosen experimental cases presented in the literature. We also presented two different hypotheses for the variation of the non-dimensional rotational diffusivity with non-dimensional fibre length, L_f/η, and Reynolds number based on the Taylor micro-scale of the turbulence, Re_λ. In terms of the Kolmogorov time and length scales, τ_η and η, and the integral scales, τ_Λ and Λ, the inverse of the adjusted non-dimensional diffusivities, $f_\eta = 1/(2D_\mathrm{r}\tau_\eta)$ and $f_\Lambda = 1/(2D_\mathrm{r}\tau_\Lambda)$, were evaluated for the different flow cases investigated. We found that assuming f_η independent of Re_λ, our data could be fitted with a weak linear dependence on the non-dimensional fibre length, L_f/η, at a relative slope of about 0.005, which is of the same order of magnitude as that of the DNS in Shin and Koch (2005) in the limit of $L_f/\eta \gg 1$. The other hypothesis neglects the effect of non-dimensional fibre length and attributes the relatively slight changes of f_η entirely to the Reynolds number, Re_λ. In this case we found that, in terms of the integral scaling, our data of $1/f_\Lambda$ could be fitted with a linear dependence on Re_λ at a slope of about 0.005–0.006, which is of the same order of magnitude as that obtained in Shin and Koch (2005) in the limit of $L_f/\Lambda \ll 1$. However, we believe that the hypothesis, which accounts for the effects of non-dimensional fibre length and is independent of Re_λ using the Kolmogorov scales for non-dimensionalization, is at an advantage, since this hypothesis in terms of the integral scaling also accounts for the effects of Reynolds number, which in turn are in a qualitative agreement with that of Shin and Koch (2005) also in the limit $L_f/\Lambda \ll 1$. To generalize our results, we will in future work determine the non-dimensional functions for the rotational diffusivity according to the mentioned hypotheses in simulations of the same cases where the local scales of turbulence in the flow field from a CFD-simulation are used rather than the scales at the inlet of the contraction. The rotational diffusivity will then not be constant, but will change according to the proposed functions $D_\mathrm{r}^\mathrm{I} = (a_1 + b_1 Re_\lambda)(2\tau_\Lambda)^{-1}$ or $D_\mathrm{r}^\mathrm{II} = (2\tau_\eta(a_2 + b_2 L_f/\eta))^{-1}$, where only the fibre length, L_f, and the empirically determined parameters a_1, b_1 and a_2, b_2 are constants throughout the flow field. Then, as the constants have been fixed at values presumably not deviating largely from what was obtained here, we will be ready to test the models for the rotational diffusivity together with CFD-simulations in new flow cases for which the parameters were not directly adjusted for optimal fit of the anisotropy.

Acknowledgements

Marko Hyensjö would like to acknowledge the financial support from Metso Paper Inc., and the Swedish Research Council.

References

Advani, S., Tucker, C., 1987. The use of tensors to describe and predict fiber orientation in short fiber composites. J. Rheol. 31, 751–784.
Akbar, S., Altan, C., 1992. On the solution of the fibre orientation in two-dimensional homogeneous flows. Polym. Eng. Sci. 32, 810–822.
Andersson, O., Steen, I. 1962. Non-uniformity on sheet structure. In: Transactions of the Symposium held at Oxford, vol. 1, pp. 771–789.
Batchelor, G.K., 1970. Slender-body theory for particles of arbitrary cross-section in stokes flow. J. Fluid Mech. 44, 419–440.
Brown, M., Parsheh, M., Aidun, C., 2006. Turbulent flow in a converging channel: effect of contraction and return to isotropy. J. Fluid Mech. 560, 437–448.
Cox, R.G., 1970. The motion of long slender bodies in a viscous fluid, part 1. General theory. J. Fluid Mech. 44, 791–810.
Folgar, F., Tucker, C., 1984. Orientation behavior of fibers in concentrated suspensions. J. Reinf. Plast. Comp. 3, 98–119.
Goldsmith, H., Mason, S., 1967. The microrheology of dispersions. Rheology: Theory and Applications. Academic.
Hyensjö, M., Dahlkild, A., Krochak, P., Olson, J., Hämäläinen, J., 2007. Modelling the effect of shear flow on fibre orientation anisotropy in a planar contraction. Nord. Pulp Pap. Res. J. 22, 376–382.
Jeffery, G., 1922. The motion of ellipsoidal particles immersed in viscous fluid. Proc. Roy. Soc. Lond. A102, 161–179.
Koch, D., 1995. A model for orientational diffusion in fiber suspensions. Phys. Fluids 7, 2086–2088.

Krushkal, E.M., Gallily, I., 1988. On the orientation distribution function of non-spherical aerosol particles in a general shear flow – ii. the turbulent case. J. Aerosol Sci. 19, 197–211.

Nordström, B., Norman, B., 1994. Influence on sheet anisotropy, formation, z-toughness and tensile stiffness of reduced feed area to a headbox nozzle. Nord. Pulp Pap. Res. J. 1, 53–59.

Norman, B., Söderberg, D. (2001). Overview of forming literature, 1990–2000. In: Transactions of the 12th Fundamental Research Symposium, Oxford, vol. 1, pp. 431–558.

Olson, J.A., 2001. The motion of fibres in turbulent flow, stochastic simulation of isotropic homogeneous turbulence. Int. J. Multiphas. Flow 27, 2083–2103.

Olson, J.A., 2002. Analytical estimate of the fibre orientation distribution in a headbox flow. Nord. Pulp Pap. Res. J. 17, 302–306.

Olson, J.A., Kerekes, R.J., 1998. The motion of fibres in turbulent flow. J. Fluid Mech. 377, 47–64.

Olson, J.A., Frigaard, I., Chan, C., Hämäläinen, J.P., 2004. Modelling a turbulent fibre suspension flowing in a planar contraction: the one-dimensional headbox. Int. J. Multiphas. Flow 30, 51–66.

Parsheh, M., Brown, M., Aidun, C., 2005. On the orientation of stiff fibres suspended in turbulent flow in a planar contraction. J. Fluid Mech. 545, 245–269.

Parsheh, M., Brown, M., Aidun, C., 2006. Variation of fiber orientation in turbulent flow inside a planar contraction with different shapes. Int. J. Multiphas. Flow 32, 1354–1369.

Roach, P., 1987. The generation of nearly isotropic turbulence by means of grids. Heat and Fluid Flow 8, 82–92.

Shin, M., Koch, D., 2005. Rotational and translational dispersion of fibres in isotropic turbulent flows. J. Fluid Mech. 540, 143–173.

Söderberg, D., Kiviranta, A. 2003. Improvement of base-ply formation through headbox modification. In: 89th Annual PAPTAC Meeting, Montreal.

Ullmar, M. 1997. Observations of fibre orientation in a headbox model at low consistency. In: Tappi Proceedings, Engineering and Papermakers Conference, p. 865.

Ullmar, M. 1998. On fibre alignment mechanisms in a headbox nozzle. Licentiate Thesis, Royal Institute of Technology, Stockholm, Sweden.

Zhang, X. 2001. Fibre orientation in a headbox. Masters Thesis, The University of British Columbia, Vancouver, Canada.